On the parameterisation of dual-continuum models for reactive transport modelling in fractured media

Paolo Trinchero[a,1], Jordi Sanglas[a], Aitor Iraola[a], Dirk Bosbach[b], Guido Deissmann[b]

[a] *AMPHOS 21 Consulting S.L., c/Veneçuela, 103, 08019 Barcelona, Spain*
[b] *Institute of Energy and Climate Research: Nuclear Waste Management (IEK-6) and JARA-CSD, Forschungszentrum Jülich GmbH, 52425 Jülich, Germany*

Abstract

In sparsely fractured rocks, the rock matrix is an important geochemical buffer and provides significant retardation to contaminants advected through the flowing fractures. Accounting for geochemical reactions and mass exchange between these two regions is key to properly capture the overall buffering capacity and the related hydrogeochemical evolution of a fractured medium. Reactive transport modelling in these kinds of fractured media is routinely performed using Equivalent Continuos Porous Media (ECPM) models: i.e. continuum models based on permeability and porosity fields that somehow preserve the underlying fracture properties, which are in turn described by companion Discrete Fracture Network (DFN) models. However, the proper parameterisation of these models, in terms of mass exchange between fractures and the bordering matrix, is still a largely unresolved issue. Here, we leverage the Dual Continuum Disconnected Matrix Model (DCDMM) formulation included in the massively parallel code PFLOTRAN to propose a novel parameterisation approach that honours the local volumetric fracture density ($P32$). The proposed approach is first benchmarked against a semi-analytical solution with a problem that entails flow and transport along two different and consecutive fractures. Two demonstrative large-scale reactive transport problems are also presented and discussed: the first is related to the generation and migration of radiogenic helium and the

---

[1] Corresponding author: paolo.trinchero@amphos21.com

second assesses the buffering capacity of a realistic fractured medium against the infiltration of acidic water. The latter simulation, which includes more than three hundred million transport degrees of freedom is one of the largest subsurface reactive transport models ever formulated and solved. This simulation was made possible by the highly efficient implementation of the DCDMM in PFLOTRAN, which makes the solution of the secondary continuum equations embarrasingly parallel.

Keywords: reactive transport modelling, fractured media, Dual-Continuum Disconnected Matrix Model, Discrete Fracture Network models

2010 MSC: 86-08, 62P12

---

1. Introduction

In crystalline rocks, fractures are typically sparse and their size is commonly described by power-law relationships (Selroos et al., 2022, and references therein), which means that most of these features are in the meter scale while larger fractures (> 10 m) are rare. Some of these fractures are hydraulically connected and form a network through which dissolved solutes may be transported by advection. Solutes may also be exchanged with the rock matrix through molecular diffusion (Neretnieks, 1980), wherefore fractured crystalline rocks effectively behaves as a dual-porosity system (Bibby, 1981). The rock matrix might play an important role as a buffer against hydro-geochemical perturbations (e.g. the infiltration of oxygenated glacial meltwater; Trinchero et al. (2017)), and can significantly retard the transport of solutes along flowing fractures (e.g. radionucles, Trinchero et al., 2020a).

Sparsely fractured crystalline rocks are often represented using Discrete Fracture Network (DFN) models, in which groundwater flow and transport are assumed to take place along a connected network of two-dimensional geometrical entities. DFNs are typically based on statistical descriptions of observable distributions such as fracture traces in outcrops or drill-cores, whereby they may be characterized by a specificed fracture intensity (Dershowitz, 1984). Each geometrical entity represents a single fracture and is characterised by its own flow, hydraulic and transport aperture. Despite being cornerstones for, e.g., safety assessment studies of nuclear waste repositories in fractured rocks, and despite increasingly accessible computational power and efficient computer codes available, the deployment of DFN models for regional-scale reactive transport modelling is still computationally prohibitive. Thus, reactive transport models are routinely based on Equivalent Continuous Porous Media (ECPM) representations of the fractured system (e.g. Wang et al., 2022a); i.e. continuum models based on heterogeneous distributions of permeability, storativity and porosity that somehow preserve the underlying fracture properties (Svensson, 2001a,b).

Though the formulation of ECPM models has been widely assessed (e.g. Jackson et al., 2000), how to represent mass exchange processes between flowing fractures and the bordering rock matrix in ECPM models is still a largely unresolved issue that requires selecting numerical schemes and appropriate parameterisation strategies. An aspect to be taken into account is computational efficiency since, depending on the chosen approach, the explicit consideration of the rock matrix might increase the total number of transport degrees of freedom by an order of magnitude, or more. Moreover, not all the available schemes of mass exchange are suited for the simulation of complex reactive transport phenomena defined by tens of primary and secondary species and by a number of primary and secondary minerals. The Multi-Rate Mass Transfer Model (Haggerty and Gorelick, 1995), which has been recently generalised to the solution of reactive problems (Wang et al., 2022b), is indeed a potentially appealing approach which however requires further testing and development since, to date, has only been applied to the simulation of simple physical and chemical systems and it has not been coded in parallel reactive transport codes. An alternative approach for the modelling of dual-porosity systems, which was formulated in the context of fluid and heat transport, is the so-called Multiple INteracting Continua (MINC) method Pruess (1985). MINC postulates a "sugar cube" model for a fractured-porous reservoir, where discontinuous cubic matrix blocks are separated by fractures. MINC was later implemented in the flow and reactive transport code TOUGHREACT (Xu et al., 2006). A very similar conceptual model is used in the so-called Dual Continuum Disconnected Matrix Model (DCDMM) (Lichtner, 2000), which is the basis for the multiple continuum module implemented into the high-performance reactive transport code PFLOTRAN (Hammond and Lichtner, 2010; Lichtner et al., 2013b). A significant difference between the two implementations is that in TOUGHREACT primary and secondary continua are handled as a single system of equations that is solved simultaneously whereas in PFLOTRAN the primary and secondary continua are solved separately by considering the secondary continua as a 1D system of equations. The latter is a significantly more computationally efficient approach (Lichtner and Karra, 2014; Iraola et al., 2019).

In this paper we show that by honoring the local fracture density when parameterising dual-continuum models, reactive transport can be efficiently simulated in fractured media using the DCDMM computational algorithm. We also demonstrate the use of this approach for simulating reactive transport in DFNs for large scale applications. A test case simulating transport between two consecutive fractures is shown to illustrate the conceptual framework and to verify the numerical implementation. Two large-scale DFN-derived ECPM reactive transport models, one focused on describing radiogenic helium production and migration and the second related to low-pH buffering by calcite dissolution, are also presented and discussed. To the knowledge of the authors, the latter simulation, which includes more than three hundred million transport degrees of freedom and was run in the supercomputer JURECA for a simulation time frame of 10,000 y, is one of the largest subsurface reactive transport models ever formulated and solved at this level of detail.

2. Mathematical development

The modelling framework discussed in this work is related to the multiple continuum module implemented in PFLOTRAN (Lichtner et al., 2013a; Hammond et al., 2014; Lichtner and Karra, 2014).

In the dual-continuum (DC) approach used in this work, the total volume V_{tot} of the fractured system is split into primary continuum volume (fracture volume, V_F) and secondary continuum volume (V_m), and the following relationship holds

$$V_{\text{tot}} = V_f + V_m. \tag{1}$$

The equation can be re-written in terms of corresponding volume fractions of the two continua

$$1 = \epsilon_f + \epsilon_m, \tag{2}$$

where ϵ is the volume fraction and the sub-scripts f, m are for fracture and matrix continua, respectively.

The representation of reactive chemical species follows the canonical form presented in Lichtner et al. (1996). If there are n reacting chemical species with n_R aqueous reactions and n_R^{eq} aqueous equilibrium reactions, then the system can be simplified by splitting it into $n_c = n - n_R^{\text{eq}}$ components or primary species and n_R^{eq} remaining secondary species. The concentrations of primary species are obtained from mass balance conservation, whereas the concentrations of the secondary species are evaluated from the primary species concentrations using law of mass action. The total component concentrations, which are the conserved quantities, are defined as:

$$\Psi_j^{f,m} = c_j + \sum_{i=1}^{n_r^{\text{eq}}} \nu_{ji}^{\text{eq}} c_i, \tag{3}$$

here j indicates the primary species, the sum is performed over the n_r^{eq} secondary species with stoichiometric coefficients ν_{ji} and c indicating the respective molar concentrations. Notice that from now on super/sub-script f, m is used to indicate that a quantity/operator applies to either the fracture (super/sub-script f) or the rock matrix (super/sub-script m).

The same set of aqueous and mineral reactions are assumed to occur in both primary and secondary continua. We refer to Lichtner and Karra (2014) and Iraola et al. (2019) for details on how aqueous and mineral reactions are re-casted in a canonical form. Assuming saturated flow conditions, the mass balance equations for the two continua take the form:

$$\frac{\partial}{\partial t}\left(\epsilon_f \varphi_f \Psi_j^f\right) + \nabla \cdot \mathbf{\Omega}_j^f = -\epsilon_f \sum_{s=1}^{n_s} \nu_{js} I_s^f + \epsilon_f \sum_{r=n_r^{\text{eq}}+1}^{n_r} \nu_{jr}^{\text{kin}} I_r^f + S^f - \mathcal{A}_{fm} \mathcal{F}^{fm}, \tag{4a}$$

$$\frac{\partial}{\partial t}\left(\varphi_m \Psi_j^m\right) + \nabla_\xi \cdot \mathbf{\Omega}_j^m = -\sum_{s=1}^{n_s} \nu_{js} I_s^m + \sum_{r=n_r^{\text{eq}}+1}^{n_r} \nu_{jr}^{\text{kin}} I_r^m + S^m, \tag{4b}$$

where $\Psi_j^{f,m}$ are the total concentrations of species j and $\varphi_{f,m}$ are the porosities of the two continua. $S^{f,m}$ are source/sink terms and $I_r^{f,m}$ are the aqueous kinetic reaction rates, in the primary and secondary continua. The operators ∇, ∇_ξ are the gradient operators in the primary and secondary continua respectively, with ξ representing the secondary continuum space. The first term on the right hand side of the two equations includes the n_s mineral kinetic reactions and $I_s^{f,m}$ are the mineral kinetic reaction rates, with respective stoichiometric coefficients ν_{js}, which are defined as:

$$I_s^{f,m} = k_s^{f,m} a_s^{f,m} \left(1 - K_s^{f,m} Q_s^{f,m}\right) \zeta_s^{f,m}, \tag{5}$$

where $k_s^{f,m}$, $a_s^{f,m}$ are the kinetic rate constants and specific mineral surface areas in the primary and secondary continua, respectively. $K_s^{f,m}$ are the equilibrium constants and $Q_s^{f,m}$ are the ion activity products given as:

$$Q_s^{f,m} = \prod_j \left(a_j^{f,m}\right)^{\nu_{js}^{f,m}}. \tag{6}$$

Eq. (6) is a function of the activities defined as the product of the species concentrations and their corresponding activity coefficients ($a_j = \gamma_j a_j$). The equilibrium constant may vary with temperature and can thus, in principle, be different in the fracture and matrix continua. The factors $\zeta_s^{f,m}$ take on the values one or zero depending on, whether the mineral is supersaturated or undersaturated and present in the control volume ($\zeta_s^{f,m} = 1$), or undersaturated but not present ($\zeta_s^{f,m} = 0$), and are calculated as follows:

$$\zeta_s^{f,m} = \begin{cases} 1, & K_s^{f,m} Q_s^{f,m} > 1 \quad \text{or} \quad \phi_s^{f,m} > 0, \\ 0, & \text{otherwise}, \end{cases} \tag{7}$$

where $\phi_s^{f,m}$ are the mineral volume fractions in the primary and secondary continua. Changes in mineral volume fractions are calculated from the mineral balance equations

$$\frac{\partial \phi_s^{f,m}}{\partial t} = \overline{V}_s I_s^{f,m}, \tag{8}$$

where $\overline{V}_s$ is the mineral molar volume.

In Eq. (4a), the mass exchange between primary and secondary continuum is given by the term $\mathcal{A}_{fm}\mathcal{F}^{fm}$, where $\mathcal{F}^{fm}$ if the mass flux, while $\mathcal{A}_{fm}$ is the fracture bulk specific surface area defined as the fracture-matrix interfacial area per bulk volume [m^{-1}]. In fractured media, $\mathcal{A}_{fm}$ is equal to twice the statistical parameter $P32$ (Dershowitz, 1984). The latter is typically used to define fracture density in DFN modelling and is expressed as the fracture surface area per unit volume. It should be noticed that a factor of 2 is needed since transport simulations and the related parameters explicitly acknowledge the existence of two surfaces, separated by the fracture volume, whereas DFN statistics treat fractures as planar entities.

Mass fluxes ($\boldsymbol{\Omega}^{f,m}$) are evaluated as:

$$\boldsymbol{\Omega}_j^f = \boldsymbol{q}^f \Psi_j^f - \epsilon_f \varphi_f \boldsymbol{D}^f \nabla \Psi_j^f, \tag{9a}$$

$$\boldsymbol{\Omega}_j^m = -\varphi_m D^m \nabla_\xi \Psi_j^m, \tag{9b}$$

where $\boldsymbol{D}^f$ is the hydrodynamic dispersion tensor in the fracture, D^m is the pore diffusion coefficient in the matrix and $\boldsymbol{q}^f$ is the water volumetric flux in the fracture calculated using Darcy's model:

$$\boldsymbol{q}^f = -\frac{k^f k_r}{\mu} \nabla \left(p^f - \rho g z \right), \tag{10}$$

where k^f is the fracture saturated permeability, k^r is the relative permeability, μ is the viscosity of water, p^f is the pore pressure of water in the fracture continuum, ρ is the water density, g is gravitational acceleration and z is the elevation. Notice that D^m in Eq. (9b) accounts for the constrictivity and tortuosity of the rock matrix and thus is typically one to several orders of magnitude lower than molecular diffusion in water.

The following boundary conditions are set on the secondary continuum:

$$\Psi_j^m \left(\xi = 0, t; \boldsymbol{x} \right) = \Psi_j^f \left(\boldsymbol{x}, t \right), \tag{11a}$$

$$\nabla_\xi \Psi_j^m \cdot \boldsymbol{n} \left(\xi = \Delta_m, t; \boldsymbol{x} \right) = 0, \tag{11b}$$

where $\boldsymbol{x}$ is a point in fracture continuum, t is time, $\xi = 0$ is the interface between fracture and matrix and Δ_m is the matrix length. Eq. (11a) implies continuity at the fracture-matrix interface whereas Eq. (11b) assumes that there is symmetry in the fracture-matrix system and $2\Delta_m$ is typically considered as the fracture spacing. Appropriate initial conditions for concentrations, that need not be identical, are prescribed in both continua. Notice that these initial and boundary conditions are imposed by the DCDMM formulation.

The primary and secondary continua are linked through the mass exchange flux term:

$$\mathcal{F}^{fm} \left(\boldsymbol{x}, t \right) = \boldsymbol{\Omega}^m \cdot \boldsymbol{n} \left(\xi = 0, t; \boldsymbol{x} \right). \tag{12}$$

In PFLOTRAN, the primary and secondary continuum mass balance partial differential equations in Eq. (4) are discretized using a two-point flux finite volume method in space and using backward Euler scheme resulting in a set of equivalent non-linear algebraic equations.

The system of partial differential equations (Eq. (4)) implies that the diffusive mass flux exchange term depends only on the given primary continuum grid cell concentration and its corresponding secondary continuum concentration, whereas it does not depend on other primary/secondary continuum grid cells. The DCDMM is particularly efficient since the boundary condition for the governing equation of the secondary continuum is only a function of the concentration at the primary grid cell that it belongs to. This implies that the primary and secondary continua are fully implicitly coupled, but the secondary continua are only solved in 1D. This coupling leads to an embarrassingly parallel system of equations for the secondary continuum.

Concentrations of primary species are obtained by solving for mass conservation for the components (Eq. (4)). Concentrations of secondary species are then retrieved from the law of mass action for the equilibrium equations:

$$K_i = \frac{a_i}{\prod_{j=1}^{n_c} (a_j)^{\nu_{ji}^{\mathrm{eq}}}}. \tag{13}$$

3. Parameterisation of DFN-based ECPM reactive transport models

There are different techniques that can be used to formulate equivalent permeability and porosity values for DFN-based ECPM models. Some of these techniques consist in performing local-scale flow and tracer experiments and from those deriving equivalent permeability tensors and porosity values (Jackson et al., 2000). Other approaches formulate these properties based on pure geometric considerations (Svensson, 2001a; McKenna and Reeves, 2006). The way how ECPM parameters are defined is not central to this work; thus a discussion on pros and cons of these different approaches is out of the scope of this study. Here, we will simply illustrate the derivation of permeability and porosity values in geometric-based methods and we use the related equations as the basis for the formulation of a DFN-consistent parameterisation of mass-exchange processes. It is worthwhile noting that the proposed formulation is generic and can be used in any DFN-based ECPM model, irrespective of the way how ECPM parameters are defined.

The equivalent permeability of the j-th grid block (k_{eq_j} [m^2]) is computed as:

$$k_{eq_j} = \frac{2}{3d} \sum_{i=1}^{N} b_i^3, \tag{14}$$

where the sum is over the N fracture intersecting the current grid block, b_i [m] is the half aperture of the i-th fracture and d [m] is the fracture spacing, which is typically set equal to the grid size (Δ_j [m]) divided by N. Some numerical codes based on the finite volume method compute fracture intersections at cell sides, thus allowing for anisotropy to be properly captured. In some other formulations, anisotropy is explicitly accounted for by means of a full permeability tensor (Hadgu et al., 2017). Regardless of the method used to represent permeability, kinematic porosity is defined as

$$\epsilon_{f_j} = \frac{2 \sum_{i=1}^{N} A_{i\cap j} b_i}{V_{b_j}}, \tag{15}$$

where $A_{i\cap j}$ [m^2] is the surface area of fracture i that intersects grid cell j and V_b [m^3] is the bulk volume of the considered grid cell. In transport applications, $2A_{i\cap j}$ is denoted as flow-wetted surface area (Moreno and Neretnieks, 1993) and is a key parameter controlling mass transfer between the flowing fracture and the bordering rock matrix. Notice that this definition of ϵ is consistent with that of fracture volume fraction defined in Eq. (2).

The dual-continuum framework presented in section 2 is defined by parameters that are a function of the underlying fracture-matrix system. Some of these parameters, such as pore diffusivity (D^m) and matrix porosity (φ_m), depend on characteristics of the rock matrix and can be determined in the laboratory by means of e.g. water saturation method and through diffusion experiments (e.g. Trinchero et al., 2020b, and references therein). The other three parameters within the dual-continuum framework are dependent on the geometry of the fracture network and the related fracture characteristics namely the fracture volume fraction (ϵ_f; Eq. (2)), the fracture bulk specific surface area ($\mathcal{A}_{fm}$; Eq. (4a)) and the matrix length (Δ_m; Eq. (11b)). It turns out that a proper parameterisation of a dual-continuum ECPM model should be carried out in a way consistent with the underlying DFN model, which is what we do next.

The fracture volume fraction has already been derived in Eq. (15) whereas the bulk specific fracture surface area is related to the local $P32$:

$$\mathcal{A}_{fm_j} = \frac{2\sum_{i=1}^{N} A_{i\cap j}}{V_{b_j}} = 2 \cdot P32. \tag{16}$$

To derive a DFN-consistent value of matrix thickness, we assume that each grid cell of the continuum model is represented as a system of parallel planar fractures. This conceptualisation implies that matrix length is the inverse of the fracture specific surface area:

$$\Delta_{m_j} = \frac{1-\epsilon_{f_j}}{\mathcal{A}_{fm_j}} \approx \frac{1}{\mathcal{A}_{fm_j}} = \frac{1}{2 \cdot P32}. \tag{17}$$

Notice that the matrix length is the distance of any point in the fracture from the no mass-flux boundary in the bordering matrix (Eq. 11b). For the parallel fractures model used here, the matrix length is equal to the fracture half spacing.

The flowchart of Figure 1) shows the different steps, along with the companion supporting information, required for the implementation and deployment of reactive transport models for the long term analysis of deep geological repositories built in fracture crystalline rock. A DFN model is first built upon a fracture recipe that honours the observed fractured statistics (obtained from e.g. outcrop analysis, core logging, etc.) (step I). Site specific scaling laws relating e.g. fracture transmissivity to fracture size, are formulated based on the calibration of in-situ hydraulic and tracer tests (step II). The upscaling of the DFN to ECPM (step III) and the parameterisation of the dual-continuum model (IV) are carried out according to the methodology described in this section. The last step (step V) involves setting up the reactive transport model using both information from site characterisation (e.g. fracture filling mineral abundance, current groundwater composition) and results from companion models (e.g. climate models, landscape models, etc.). This flowchart is here showed with illustrative purposes only. Models are in fact fit-for-purpose and thus different steps can be followed for their implementation. No matter what these steps are, if a continuum approach is to be used, steps III and IV are deemed to be generic and thus can be used for any other application at hand.

4. Model verification

The DCDMM included in the standard release version of PFLOTRAN has limited flexibility in terms of model parameterisation, as fracture-matrix parameters are assumed to be constant across the whole model domain. Therefore, the numerical implementation of the proposed conceptual framework (sections 2 to 3) has required the development of a customised PFLOTRAN version, which allows grid-cell based values of ϵ_f and Δ_m to be accommodated using external hdf5 files. Notice that, as already discussed, $\mathcal{A}_{fm_j}$ is inversely dependent on matrix thickness. In this section, the robustness of the conceptual framework as well as the correct implementation of the DCDMM are verified by solving a simplified exercise based on transport along two consecutive fractures. Results are compared with an independent solution.

In sparsely fractured media, solute transport is typically assumed to occur along a network of inter-connected fracture segments, where each segment is characterised by its own fracture aperture and groundwater residence time (Trinchero et al., 2020a). Using this conceptualisation, in this verification exercise two consecutive intersecting fracture segments are considered, and a hydraulic gradient is applied between the inlet boundary of the upstream fracture (UF) and the outlet boundary of the downstream fracture (DF). The fracture-matrix system is initially tracer free and a Dirichlet boundary condition is used to set a constant tracer concentration at the inlet of the UF. The considered solute is non-sorbing and non-decaying. The DF is characterised by a wider aperture ($b^{DF} = 2b^{UF}$) and the two fractures are mapped into an ECPM using

Eq. (14) and (15). It is assumed that both fractures see the same extent of rock matrix ($\Delta_m^{UF} = \Delta_m^{DF}$) thus $k_{eq}^{DF} = 8k_{eq}^{UF}$ and $\epsilon_{eq}^{DF} \approx 2\epsilon_{eq}^{UF}$. The parameters of the fracture-matrix system are summarised in Table 1, whereas the corresponding parameters of the ECPM and related boundary conditions are listed in Table 2. These continuum-based models were built and solved using PFLOTRAN.

The average permeability of the whole system is given by the harmonic mean:

$$\overline{k} = \frac{2k_{eq}^{UF} k_{eq}^{DF}}{k_{eq}^{UF} + k_{eq}^{DF}}. \tag{18}$$

Notice that this average permeability is here only used to compute the average groundwater travel time, which is equal to $\overline{\tau} = 1.76 \cdot 10^{-2}$ y.

The results of the PFLOTRAN calculation are here compared to the analytical solution developed by Sudicky and Frind (1982) (Sudicky's solution, for the sake of brevity). Sudicky's solution is based on a system of parallel homogeneous fractures. However, it can be easily extended to account for longitudinal changes in aperture and velocity by using the convolution theorem in Laplace space (see Appendix A for further details). The flow-related parameters used for Sudicky's solution are listed in Table 3. The others parameters used for the Sudicky's solution are the same as listed in Table 1. An additional continuum-based PFLOTRAN simulation was carried out in which matrix diffusion was not considered. In all the models a continuous injection of a conservative tracer is simulated.

Breakthrough curves showing the computed normalised concentration at the fracture outlet ($\mathrm{C/C_0}$) are shown in Figure 2 top. From the logarithmic plot of $1 - \mathrm{C/C_0}$ (Figure 2 bottom) it can be noticed that all the breakthrough curves display the expected -0.5 late-time slope except for the simulation without matrix that has no tail. The agreement between the dual-continuum ECPM model and the Sudicky's solution is very good. A small dispersion has been used in the latter (Table 3) to account for the small numerical dispersion introduced by PFLOTRAN. This good agreement confirms the correct implementation of the cell-based parameterisation of the dual-continuum model of PFLOTRAN and supports the parameterisation approach proposed in section 3. It is worth noting that, except for the simulation without matrix diffusion, all the other solutions display the same height of the tail. As shown by Trinchero et al. (2020b), the height of the tail depends on the product of a material parameter group (see Appendix A and Eq. A.4) and a flow-related parameter called transport resistance, which is defined as the ratio between the groundwater travel time and the fracture half aperture ($\beta = \tau/b$) (Cvetkovic et al., 1999). All the considered models, including the two homogeneous cases, have the same material parameter group and also the same transport resistance, since the wider aperture of the DF compensates its longer groundwater travel time. It is also worthwhile noting that late-time tails are not affected by matrix limitation. This is because the considered time frame (0.1 y) is much shorter than the characteristic time needed by tracer front to reach the outer matrix boundary ($t_c = \Delta_m^2/D^m \sim 3.2$ y).

An additional verification is presented in Appendix B, where the results computed using the DCDMM are compared with calculations performed using the time-domain random walk computer code MARFA (Painter et al., 2008; Painter and Mancillas, 2013; Trinchero et al., 2020a).

5. Large-scale applications

Here, we use the conceptual and numerical framework presented in sections 2 to 3 to show and discuss the results of two large-scale applications. The scope of these two application cases is illustrative, i.e. we aim here at showing how the proposed parameterisation approach can be employed in large-scale modelling. The presented numerical framework can be applied to a broad range of problems; therefore we have considered here two different scenarios. The first application case assesses the production and migration of radiogenic helium. The analysis of helium levels is often used for groundwater age dating in the context of safety assessment studies for deep geological repositories of nuclear waste. The second application deals with the infiltration of acidic water and is a problem that is often found in the context of acid mine drainage. Since both applications are based on the same DFN and groundwater flow model, the model set-up is presented first.

5.1. Model set-up

The DFN model used for the two large-scale applications is loosely based on a DFN model developed for the Laxemar site in Sweden (Vidstrand et al., 2010). Laxemar was one of the two sites that were thoroughly characterised during the siting process for a deep geological repository for spent nuclear fuel in Sweden (the second site, Forsmark, was finally chosen as the site for the proposed repository). The Laxemar site is located on the Swedish east coast c. 350 km south of Stockholm. The site is dominated by a geological unit known as the Transscandinavian Igneous Belt (TIB). The bedrock is characterised by intrusive rocks which have been subjected to repeated phases of brittle deformation, under varying regional stress regimes, involving reactivation along earlier formed structures (Söderbäck, 2008). Compared to Forsmark, the Laxemar site is characterised by a higher fracture frequency (particularly at repository depth, ~ 400 m).

The reason for using Laxemar is that the site was well studied during the siting process and as such the fracture recipe used here was formulated based on a comprehensive characterisation data-set; thus it is deemed to be representative of a real granitic rock system. The groundwater flow model used here should however be considered as synthetic.

The DFN was generated using the computer code DarcyTools (Svensson and Follin, 2010; Svensson and Ferry, 2014). In DarcyTools stochastic fractures are generated according to the following equation:

$$n = \frac{I}{a}\left[\left(\frac{l+dl}{l_{ref}}\right)^{a} - \left(\frac{l}{l_{ref}}\right)^{a}\right], \tag{19}$$

where n is the number of fractures per unit volume, I [m^{-3}] is the intensity, a [–] is the power law exponent and l_{ref} [m] is the reference length, which is here set to 1 m here. Fracture orientation follows a Fisher distribution characterised by the following parameters:

$$\lambda_1 = -\cos(90 - tr)\cos(pl)\kappa, \tag{20a}$$

$$\lambda_2 = -\sin(90 - tr)\cos(pl)\kappa, \tag{20b}$$

$$\lambda_3 = -\sin(pl)\kappa, \tag{20c}$$

where tr and pl are the mean trend and mean plunge, respectively, and κ is the Fisher concentration.

The following power-law relationship between fracture transmissivity (T_f [m^2/s]) and fracture size (l [m]) is considered:

$$\log(T_f) = \log\left[a_T\left(\frac{l}{100}\right)^{b_T}\right] + d_T U\left[-0.5, 0.5\right], \tag{21}$$

where a_T [m^2/s] is the transmissivity of a fracture of size $l = 100$ m and b_T [-] is the power-law exponent. U is the uniform distribution and d_T [-] is a scaling factor.

The parameters of this model are taken from the shallow part of the Hydraulic Rock Domain (HRD) of the Laxemar model (Vidstrand et al., 2010) and are summarised in Tables 4 and 5.

The considered model domain is a regular rectangular parallelepiped, with the opposite vertices located at (0.0;0.0;-128.0) and (1024.0;1024.0;0.0), with coordinates being expressed in meters. The DFN was upscaled into a structured grid of size $\Delta_x = \Delta_y = 4$ m and $\Delta_z = 2$ m, with a total number of 4,194,304 grid cells. The geometric upscaling was performed using the method specified in Svensson (2001a). Figure 3 shows the resulting spatial distribution of fracture volume fraction (ϵ_f) and Figure 4 shows the distribution of matrix length (Δ_m). The model input files generated by DarcyTools were imported into PFLOTRAN using a dedicated interface called iDP (Molinero et al., 2015).

Some of the grid cells of the ECPM are not intersected by any fracture. These cells, which are denoted here as unfractured domain (to distinguish them from the rock matrix that is part of the secondary overlapping continuum), are assigned a minimum value of permeability $\kappa = 10^{-20}\text{m}^2$, fracture volume fraction $\epsilon_f = 10^{-10}$ and a maximum matrix length equal to 4 m and are part of the numerical calculations. Sensitivity analyses carried out by deactivating the grid cells of the unfractured domain have shown that this part of the domain has a negligible effect on reactive transport across the flowing regions. The results of these sensitivity simulations are not included here for the sake of brevity.

Constant hydraulic pressure was applied to two narrow regions in the uppermost face of the domain: $p(0:10, y, 0) = p_{in}$ and $p(1014:1024, y, 0) = p_{out}$ with $p_{in} - p_{out} = 1000$ Pa. The rest of the boundaries were considered as no-flow boundaries. The secondary overlapping continuum consists of 20 cells per each cell in the primary continuum. The synthetic parameters used in this model are summarised in Table 6.

Fractured media are typically investigated by drilling deep boreholes. Since hydro-chemical measurements performed in open boreholes provide limited information for site understanding, transmissive sections are typically identified by means of flowmeters and sampling campaigns are subsequently carried out in packed-off sections of a few meters length (SKB, 2013). To mimic this situation, here four virtual boreholes have been postulated and are denoted according to their spatial location (US: upstream south, UN: upstream north, DS: downstream south, DN: downstream north). The locations of the boreholes are shown in Figure 3. Each grid cell of a given borehole represents a packed-off section and simulation results are shown and analysed accordingly. Cells belonging to the unfractured domain are not included in the analyses.

5.2. Application#1: Helium generation due to uranium and thorium decay

Fractured crystalline rocks contain a certain amount of uranium- and thorium-bearing minerals which, due to radioactive decay, produce naturally occurring radionuclides. Some of these daughter nuclides are unstable (e.g. radium and radon) while some others (i.e. the end-member of a decay chain) are stable. Helium-4 is a stable non-sorbing and non-reactive isotope and is the direct product of alpha-decay of the uranium and thorium decay series. Thus studying the production and migration of helium-4 is of particular interest for applications such as groundwater age dating (Torgersen, 1980; Bethke et al., 1999; Bethke and Johnson, 2008; Trinchero et al., 2019a; Trinchero and Iraola, 2020).

In this application, we use the model developed in section 5.1 to simulate the production of helium-4 in the rock matrix, its diffusion into the adjacent flowing fractures and its advection-driven transport.

In the simulation, besides helium, a conservative non-sorbing species was also included. Helium-4 free water was assumed to infiltrate through the inlet boundary. To keep track of conservative transport patterns, the conservative tracer was added to the infiltrating boundary water. Overall, the simulation consists of 4,194,304 x 21 x 2= 176,160,768 transport degrees of freedom. The calculation was carried out in the supercomputer JURECA of the Jülich Supercomputing Centre (Jülich Supercomputing Centre, 2018) using 680 processor cores for a total of 100,000 years of simulation time. A total of approximately 195,000 h of supercomputing allocation time was consumed. Besides the use of such a large-scale supercomputing facility, this very large simulation was feasible also thanks to the afore-discussed remarkable efficiency of the DCDMM.

To analyse the effect of matrix diffusion on the transport and retention of the conservative tracer, an additional calculation was carried out where the secondary continuum was not included. The results of the two calculations are shown in Figure 5, in form of snapshots of concentration distribution at time 1,000 y and 10,000 y. The tracer infiltrates and is primarily transported along transmissive fractures and later reaches less conductive zones of the primary continuum. For the simulation without matrix diffusion, after 100 y the tracer has reached the outlet boundary, and after 1,000 y it has reached most of the domain. In the model, matrix diffusion has a significant effect on the retardation of the tracer penetration and after 10,000 y the solute has reached only few of the cells at the outlet boundary.

Breakthrough curves of helium concentration in four randomly selected packed-off sections of the boreholes are shown in Figure 6. The four packed-off sections show a similar behaviour, with helium concentrations increasing until reaching a steady-state value. The time needed to reach this steady-state value is considerably long due to diffusion limitations. The plateau value reached by each breakthrough curve is directly proportional to the groundwater travel time, from the inlet, and inversely proportional to the fracture volume fraction (Trinchero et al., 2019a). The dependence with travel time explains why higher concentrations of helium are generally observed for the sections located in the downstream boreholes. Variability between sections located at the same distance from the inlet boundary are due to the high heterogeneity of the fractured medium, which leads to tortuos and complex infiltration pathways.

Figure 7 mimics a typical set of data available from hydrogeochemical investigations of fractured crystalline bedrock for siting of a spent nuclear fuel repository, where groundwater samples are taken from hydraulically isolated transmissive sections of available boreholes. Related hydrogeochemical measurements (in this case values of helium concentration computed at time $t=1 \cdot 10^5$ y) can be plotted against the measured values of permeability of the given packed-off sections or their depth. The results of this study indicate that the two downstream boreholes generally see higher helium concentration values because they are located further away from the inlet boundary. The results do not show any clear long-range correlation of concentration with permeability or depth. This is not surprising since helium concentration measurements are non-local: they depend on the history of the analysed groundwater sample since it has entered the subsurface (Trinchero et al., 2019a). This means that the measured helium concentration not only depends on the local value of permeability but also on its hydraulic connectivity with the inlet boundary. Helium data show a certain short-range correlation with depth. This is also not surprising since nearby sections are more likely to be affected by similar infiltration pathways. However, the significant heterogeneity of the medium is evident from the set of measurements of DN, where high concentration values ($5 \cdot 10^{-4}$ mol/L) are found at 83 m depth while distinctively lower values ($1.6 \cdot 10^{-4}$ mol/L) are found in a nearby section below (91 m depth). DS shows an opposite behaviour with very similar concentration values observed along the entire depth, which indicates that the entire borehole is affected by similar infiltration patterns.

5.3. Application#2: buffering of low pH water by calcite dissolution

The geochemical processes considered in the second application case are based on the benchmark problem presented in Iraola et al. (2019) for a single fracture-matrix system. Calcite is assumed to be initially present in the matrix ($\phi^m_{calc} = 1 \cdot 10^{-5}$) and absent in the fracture ($\phi^f_{calc} = 0$), and calcite dissolution follows the reaction:

$$\mathrm{CaCO_3} + \mathrm{H^+} \rightleftharpoons \mathrm{Ca^{2+}} + \mathrm{HCO_3^-}, \tag{22}$$

with equilibrium constant $\log K^f_s = \log K^m_s = 1.85$. The system is fully defined by the three primary species and the mineral phase of Eq. (22) and secondary species (aqueous complexes) are not included in the model. The calcite kinetic rate was set equal to $1.0 \cdot 10^{-6}$ mol/m^{2}s (Jordan and Rammensee, 1998) and a calcite specific surface area of 1 m^2/m^3 was used.

The system (i.e. both primary and secondary continua) is initially filled with a slightly alkaline water (pH=8) in equilibrium with calcite (*resident water* in Table 7) whereas a slightly acidic and calcite undersaturated water (*boundary water* in Table 7) infiltrates through the inlet boundary. The model parameterisation (e.g. permeability, fracture volume fraction, fracture length, flow boundary conditions, etc.) is the same as used in application#1.

Conceptually, the infiltration of acidic water from the inlet boundary brings acidity into the system, first through the flowing fractures, which are represented by the primary continuum. Acidity later diffuses into the rock matrix due to the existing chemical gradient between resident and boundary water. Thus, matrix diffusion represents a sink term for the acidity. In the absence of geochemical reactions, this sink term would progressively vanish once the pore water in the matrix is equilibrated with the fracture-filling water. In practice, close to the inlet boundary these coupled diffusive processes lead to calcite under-saturation in the rock matrix bordering the fractures where Eq. (22) proceeds from the left to the right. The consumption of acidity maintains the chemical gradient and the related sink term in the primary continuum. Significant changes in this system are expected to occur only when calcite is progressively depleted.

The PFLOTRAN calculation was carried out in the supercomputer JURECA (Jülich Supercomputing Centre, 2018) of the Jülich Supercomputing Centre and the simulation time frame was 10,000 years. The model discretisation is the same as described in section 5.1 and used in application#1, with the difference that here four primary species are included, which implies that the simulation involves a total of 352,321,536 transport degrees of freedom. The simulation was run using 680 processor cores and a total of 490,000 hours of supercomputing time was used.

Snapshots of pH computed at 100 y and 10,000 y are shown in Figure 8. For visualisation purposes, here only cells with $\epsilon_f > 10^{-6}$ are shown. Low pH water is only found in close proximity to the inlet boundary and a modest additional penetration is seen from 100 y to 10,000 y, which clearly indicates that acidity is strongly buffered by matrix diffusion and the related calcite dissolution processes in the rock matrix.

A detailed analysis of the chemical profiles in the rock matrix was performed considering a section of borehole B5 (Figure 3), which is located close to the inlet boundary. The considered section is at depth -45 m. The profiles of tracer concentration are shown in Figure 9 whereas the profiles of calcium, bicarbonate, pH and calcite consumption are shown in Figure 10. For all the considered species and geochemical variables profiles are shown at time 1,000 y and 10,000 y.

From Figure 9 it can be seen that, at the end of the simulation, the rock matrix is close to equilibrium with the inflowing bourdary water that contains the tracer. This is not surprising since the chosen section is located close to the inlet boundary and the chosen tracer behaves as a non-sorbing non-decaying species.

The analysis of the reactive system (Figure 10) shows that, in the considered borehole section, after 1,000 y calcite is modestly depleted in a narrow fringe close to the fracture-matrix interface. Calcite dissolution leads to an increase of calcium and bicarbonate concentrations that diffuse beyond the reaction front. Very modest changes in pH are observed as a result of calcite buffering. At the end of the simulation (10,000 y), calcite is completely depleted in the first few millimeters of the matrix, which explains the modest drop in pH, calcium and bicarbonate concentrations behind the reaction front.

The penetration depth of the reaction front at the end of the simulation is very limited and this is related to diffusion limitations, which are confirmed by an analysis of the related Damköhler number (Lichtner and Kang, 2007):

$$Da_{II} = \sqrt{\frac{K_s a_s l_c^2}{\phi^m D^m C_0}}. \tag{23}$$

Here the characteristic length has been set approximately equal to penetration depth ($l_c = 1.0 \cdot 10^{-2}$ m) and C_0 is set equal to the calcium concentration in the resident water (Table 7). These parameters give $Da_{II} = 13.8$ which further confirms that the reaction front in the rock matrix is diffusion controlled.

6. Discussion and conclusions

We have presented a conceptual framework for the parameterisation of DFN-based ECPM reactive transport models of fractured media and discussed its numerical deployment using the existing massively parallel code PFLOTRAN. The framework is suited for geological media displaying a dual-porosity behaviour; i.e. systems where groundwater flow occurs in a sparse network of connected fractures whereas the bordering rock matrix is accessible by dissolved solutes through molecular diffusion only. The study leads to the following general conclusions and recommendations:

1. Evidence from natural analogues studies (Chapman et al., 1991; Nordstrom et al., 1992; Romero et al., 1992; Cramer and Smellie, 1994; Cera et al., 2002; Akagawa et al., 2006) and from lab and site investigation programs (SKB, 2010; Poteri et al., 2017a,b) has pointed out that in sparsely

fractured media, the rock matrix plays a key role for the retardation of harmful contaminants, such as radionuclides, and is also an important geochemical buffer against possible perturbations, such as the infiltration of acidic water from the surface.

2. Continuum-based ECPM representations of the fractured media are numerically appealing formulations for reactive transport modelling.
3. Given 1) and 2), ECPM models must explicitly account for mass-exchange between the flowing fractures and the rock matrix as well as for geochemical reactions in both regions.
4. Given 3), the Dual Continuum Disconnected Matrix Model (DCDMM) is an appealing approach for large-scale reactive transport modelling in fractured media, since the secondary continuum solve is embarassingly parallel.
5. Given 3), the parameterisation of the DCDMM needs to be consistent with the underlying statistics of the fractured medium, which are typically formalised into a Discrete Fracture Network model. This consistency is here ensured by preserving the local fracture volume fraction and fracture bulk specific surface area

A verification exercise, based on two consecutive fracture segments, has been used to check both the conceptual robustness of the parameterisation approach and the proper implementation of the parameterisation strategy in the chosen numerical code. Demonstrative simulations carried out using PFLOTRAN in the super-computer JURECA have shown the suitability of the proposed approach for large-scale reactive transport modelling in sparsely fractured rocks.

A simplification of the presented large-scale models is that both geochemical reactions and transport properties are assumed to be constant through the entire rock matrix. In real fractured systems, the matrix bordering a flowing fracture might have experienced significant alteration and this might have enhanced or decreased diffusive mass exchanges (e.g. Wogelius et al., 2020). Moreover, geochemical reactions depend on the availability of relevant minerals, which might be sparsely available across the rock matrix (Trinchero et al., 2019b). In summary, both matrix and fracture internal heterogeneity might have an impact on the hydrogeochemical evolution of a fractured system. This impact should be addressed quantitatively using fit-for-purpose numerical models, which might in proncipie be based on the DCDMM formulation presented here.

Acknowledgements

The authors gratefully acknowledge the computing time granted by the JARA Vergabegremium and provided on the JARA Partition part of the supercomputer JURECA at Forschungszentrum Jülich. PT, JS and AI thank the Svensk Kärnbränslehantering AB (SKB) for the financial support. DB and GD acknowledge financial support provided by the German Federal Ministry of Education and Research (BMBF, grant agreement 02NUK053A) and the Initiative and Networking Fund of the Helmholtz Association (HGF grant SO-093) within the collaborative project iCross. The authors are gratefully indebted to Ignasi Puigdomenech for encouragement and advice throughout the work. The authors also thank Albin Nordström for his very helpful comments.

References

Akagawa, F., Yoshida, H., Yogo, S., Yamomoto, K., 2006. Redox front formation in fractured crystalline rock: an analogue of matrix diffusion in an oxidizing front along water-conducting fractures. Geochemistry: Exploration, Environment, Analysis 6, 49–56.

Bethke, C.M., Johnson, T.M., 2008. Groundwater age and groundwater age dating. Annual Review of Earth and Planetary Sciences 36, 121–152. URL: `https://doi.org/10.1146/annurev.earth.36.031207.124210`, doi:`10.1146/annurev.earth.36.031207.124210`, `arXiv:https://doi.org/10.1146/annurev.earth.36.031207.124210`.

Bethke, C.M., Zhao, X., Torgersen, T., 1999. Groundwater flow and the ^{4}He distribution in the Great Artesian Basin of Australia. Journal of Geophysical Research: Solid Earth 104, 12999–13011. URL: `https://agupubs.onlinelibrary.wiley.com/doi/abs/10.1029/1999JB900085`, doi:`https://doi.org/10.1029/1999JB900085`, `arXiv:https://agupubs.onlinelibrary.wiley.com/doi/pdf/10.1029/1999JB900085`.

Bibby, R., 1981. Mass transport of solutes in dual-porosity media. Water Resources Research 17, 1075–1081. URL: `http://dx.doi.org/10.1029/WR017i004p01075`, doi:`10.1029/WR017i004p01075`.

Cera, E., Ahonen, L., Rollin, C., Bruno, J., Kaija, J., Blomqvist, R., 2002. Redox processes at the Palmottu uranium deposit. The Palmottu Natural Analogue Project. Technical Report Y50/99/19. Geological Survey of Finland.

Chapman, N., McKinley, I., Shea, M., Smellie, J., 1991. The Poços de Caldas Project: Summary and implications for radioactive waste management. Technical Report TR-90-24. Svensk Kärnbränslehantering AB (SKB), Stockholm, Sweden.

Cramer, J., Smellie, J., 1994. Final report of the AECL/SKB Cigar Lake analog study. Technical Report TR-94-04. Svensk Kärnbränslehantering AB (SKB), Stockholm, Sweden.

Cvetkovic, V., Selroos, J., Cheng, H., 1999. Transport of reactive tracers in rock fractures. Journal of Fluid Mechanics 378, 335–356.

De Hoog, F.R., Knight, J., Stokes, A., 1982. An improved method for numerical inversion of Laplace transforms. SIAM Journal on Scientific and Statistical Computing 3, 357–366.

Dershowitz, W.S., 1984. Rock joint systems. Ph.D. thesis. Massachusetts Institute of Technology.

Hadgu, T., Karra, S., Kalinina, E., Makedonska, N., Hyman, J.D., Klise, K., Viswanathan, H.S., Wang, Y., 2017. A comparative study of discrete fracture network and equivalent continuum models for simulating flow and transport in the far field of a hypothetical nuclear waste repository in crystalline host rock. Journal of Hydrology 553, 59–70. URL: `https://www.sciencedirect.com/science/article/pii/S0022169417305115`, doi:`https://doi.org/10.1016/j.jhydrol.2017.07.046`.

Haggerty, R., Gorelick, S.M., 1995. Multiple-rate mass transfer for modeling diffusion and surface reactions in media with pore-scale heterogeneity. Water Resources Research 31, 2383–2400.

Hammond, G., Lichtner, P., Mills, R., 2014. Evaluating the performance of parallel subsurface simulators: An illustrative example with PFLOTRAN. Water Resources Research 50, 208–228.

Hammond, G.E., Lichtner, P.C., 2010. Field-scale model for the natural attenuation of uranium at the Hanford 300 area using high-performance computing. Water Resources Research 46, W09527, 1–31.

Hollenbeck, K., 1998. INVLAP. M: A matlab function for numerical inversion of Laplace transforms by the de Hoog algorithm. http://www. isva. dtu. dk/staff/karl/invlap. htm .

Iraola, A., Trinchero, P., Karra, S., Molinero, J., 2019. Assessing dual continuum method for multicomponent reactive transport. Computers & Geosciences 130, 11–19. URL: `http://www.sciencedirect.com/science/article/pii/S0098300418307982`, doi:`https://doi.org/10.1016/j.cageo.2019.05.007`.

Jackson, C.P., Hoch, A.R., Todman, S., 2000. Self-consistency of a heterogeneous continuum porous medium representation of a fractured medium. Water Resources Research 36, 189–202.

URL: `https://agupubs.onlinelibrary.wiley.com/doi/abs/10.1029/1999WR900249`, doi:`https://doi.org/10.1029/1999WR900249`, `arXiv:https://agupubs.onlinelibrary.wiley.com/doi/pdf/10.1029/1999WR900249`.

Jordan, G., Rammensee, W., 1998. Dissolution rates of calcite (1014) obtained by scanning force microscopy: microtopography-based dissolution kinetics on surfaces with anisotropic step velocities. Geochimica et Cosmochimica Acta 62, 941–947.

Jülich Supercomputing Centre, 2018. JURECA: Modular supercomputer at Jülich Supercomputing Centre. Journal of large-scale research facilities 4. URL: `http://dx.doi.org/10.17815/jlsrf-4-121-1`, doi:`10.17815/jlsrf-4-121-1`.

Lichtner, P., Hammond, G., Lu, C., Karra, S., Bisht, G., Andre, B., Mills, R., Kumar, J., 2013a. PFLOTRAN Web page. Http://www.pflotran.org.

Lichtner, P., Hammond, G.E., Lu, C., Karra, S., Bisht, G., Andre, B., Mills, R., Kumar, J., 2013b. PFLOTRAN User Manual. Technical Report.

Lichtner, P.C., 2000. Critique of dual continuum formulations of multicomponent reactive transport in fractured porous media. Dynamics of fluids in fractured rock, Geophysical Monograph Series 122 , 281–298.

Lichtner, P.C., Kang, Q., 2007. Upscaling pore-scale reactive transport equations using a multiscale continuum formulation. Water Resources Research 43. URL: `https://agupubs.onlinelibrary.wiley.com/doi/abs/10.1029/2006WR005664`, doi:`https://doi.org/10.1029/2006WR005664`, `arXiv:https://agupubs.onlinelibrary.wiley.com/doi/pdf/10.1029/2006WR005664`.

Lichtner, P.C., Karra, S., 2014. Modeling multiscale-multiphase-multicomponent reactive flows in porous media, In: Al-Khoury, R., Bundschuh, j (eds.): Application to CO_2 sequestration and enhanced geothermal energy using PFLOTRAN. Computational Models for CO_2 Geo-sequestration & Compressed Air Energy Storage, CRC Press, London. , 81–136.

Lichtner, P.C., Steefel, C.I., Oelkers, E.H., 1996. Reactive transport in porous media. De Gruyter, Berlin, Boston. URL: `https://www.degruyter.com/view/title/537284`, doi:`https://doi.org/10.1515/9781501509797`.

McKenna, S., Reeves, P., 2006. Fractured continuum approach to stochastic permeability modeling. In: Coburn, T. C., Yarus, J. M., Chambers, R. L. (eds.) Stochastic Modeling and Geostatistics: Principles, Methods, and Case Studies, Volume II. American Association of PetroleumGeologists,DOI: https://doi.org/10.1306/CA51063. .

Molinero, J., Trinchero, P., Ebrahimi, H., de Vries, L., Luna, M., Svensson, U., Lichtner, P., 2015. The BRIDGE Project: Development, testing and application of a high performance computing framework for reactive transport modelling in crystalline roks (iDP). Technical Report R-15-17. Svensk Kärnbränslehantering AB, Stockholm, Sweden.

Moreno, L., Neretnieks, I., 1993. Flow and nuclide transport in fractured media: The importance of the flow-wetted surface for radionuclide migration. Journal of Contaminant Hydrology 13, 49–71. URL: `http://www.sciencedirect.com/science/article/pii/0169772293900503`, doi:`https://doi.org/10.1016/0169-7722(93)90050-3`. chemistry and Migration of Actinides and Fission Products.

Neretnieks, I., 1980. Diffusion in the rock matrix: an important factor in radionuclide retardation. Journal of Geophysical Research 85, 4379–4397.

Nordstrom, D., McNutt, R., Puigdomènech, I., Smellie, J.A., Wolf, M., 1992. Ground water chemistry and geochemical modeling of water-rock interactions at the Osamu Utsumi mine and the Morro do Ferro analogue study sites, Poços de Caldas, Minas Gerais, Brazil. Journal of Geochemical Exploration 45, 249–287.

Painter, S., Cvetkovic, V., Mancillas, J., Pensado, O., 2008. Time domain particle tracking methods for simulating transport with retention and first-order transformation. Water Resources Research 44(1), W014061.

Painter, S., Mancillas, J., 2013. MARFA user's manual: Migration analysis of radionuclides in the far field. Technical Report POSIVA Working Report 2013-01. Posiva Oy, Helsinki, Finland.

Poteri, A., Andersson, O., Nilsson, K., Byegård, J., Skålberg, M., Siitari-Kauppi, M., Helariutta, K., Voutilainen, M., Kekäläinen, P., 2017a. The first matrix diffusion experiment in the water phase of the REPRO Project: WPDE 1. Technical Report Workreport 2017-24. Posiva Oy, Eurajoki, Finland.

Poteri, A., Andersson, O., Nilsson, K., Byegård, J., Skålberg, M., Siitari-Kauppi, M., Helariutta, K., Voutilainen, M., Kekäläinen, P., Ikonen, J., Sammaljärvi, J., Lindberg, A., Timonen, J., Kuva, J., Koskinen, L., 2017b. The second matrix diffusion experiment in the water Phase of the REPRO Project: WPDE 2. Technical Report Workreport 2017-23. Posiva Oy, Eurajoki, Finland.

Pruess, K., 1985. A practical method for modeling fluid and heat flow in fractured porous media. Society of Petroleum Engineers Journal 25, 14–26. URL: `https://doi.org/10.2118/10509-PA`, doi:`10.2118/10509-PA`.

Romero, L., Neretnieks, I., Moreno, L., 1992. Movement of the redox front at the Osamu Utsumi uranium mine, Poços de Caldas, Brazil. Journal of Geochemical Exploration 45, 471–502.

Selroos, J.O., Mas Ivars, D., Munier, R., Hartley, L., Libby, S., Davy, P., Darcel, C., Trinchero, P., 2022. Methodology for Discrete Fracture Network modelling of the Forsmark site. Part 1 â€“ concepts, data and interpretation methods. Technical Report R-20-11. , Svensk KÃ¤rnbrÃ¤nslehantering AB (SKB), Solna, Sweden.

SKB, 2010. Radionuclide transport report for the safety assessment SR-Site. Technical Report TR-10-50. Svensk Kärnbränslehantering AB (SKB), Stockholm, Sweden.

SKB, 2013. Site-descriptive modelling for a final repository for spent nuclear fuel in Sweden. Main report of the SR-Site project. Technical Report TR-11-01. Svensk Kärnbränslehantering AB (SKB), Stockholm, Sweden.

Söderbäck, B.e., 2008. Geological evolution, palaeoclimate and historical development of the Forsmark and Laxemar-Simpevarp areas. Site descriptive modelling SDM-Site. Technical Report R-08-19. Svensk Kärnbränslehantering AB (SKB), Stockholm, Sweden.

Sudicky, E.A., Frind, E., 1982. Contaminant transport in fractured porous media: Analytical solution for a system of parallel fractures. Water Resources Research 18, 1634–1642.

Svensson, U., 2001a. A continuum representation of fracture networks. Part I: Method and basic test cases. Journal of Hydrology 250, 170–186.

Svensson, U., 2001b. A continuum representation of fracture networks. Part II: Application to the Äspö Hard Rock laboratory. Journal of Hydrology 250, 187–205.

Svensson, U., Ferry, M., 2014. DarcyTools: a computer code for hydrogeological analysis of nuclear waste repositories in fractured rock. Journal of Applied Mathematics and Physics 2, 365.

Svensson, U., Follin, S., 2010. Groundwater flow modelling of the excavation and operational phases-Forsmark. Technical Report R-09-19. Svensk Kärnbränslehantering AB (SKB), Stockholm, Sweden.

Torgersen, T., 1980. Controls on pore-fluid concentration of ^{4}He and ^{222}Rn and the calculation of ^{4}He/^{222}Rn ages. Journal of Geochemical Exploration 13, 57–75. URL: `http://www.sciencedirect.com/science/article/pii/0375674280900217`, doi:`https://doi.org/10.1016/0375-6742(80)90021-7`.

Trinchero, P., Iraola, A., 2020. Models for the assessment of transport of naturally-occurring nuclides in fractured media. Journal of Hydrology 580, 124322. URL: `http://www.sciencedirect.com/science/article/pii/S0022169419310571`, doi:`https://doi.org/10.1016/j.jhydrol.2019.124322`.

Trinchero, P., Painter, S.L., Poteri, A., Sanglas, J., Cvetkovic, V., Selroos, J.O., 2020a. A particle-based conditional sampling scheme for the simulation of transport in fractured rock with diffusion into stagnant water and rock matrix. Water Resources Research 56, e2019WR026958. URL: `https://agupubs.onlinelibrary.wiley.com/doi/abs/10.1029/2019WR026958`, doi:`https://doi.org/10.1029/2019WR026958`, `arXiv:https://agupubs.onlinelibrary.wiley.com/doi/pdf/10.1029/2019WR026958`. e2019WR026958 10.1029/2019WR026958.

Trinchero, P., Poteri, A., Gylling, B., Selroos, J.O., 2020b. Modelling the water phase diffusion experiment at Onkalo (Finland): Insights into the effect of channeling on radionuclide transport and retention. Journal of Hydrology 590, 125399. URL: `http://www.sciencedirect.com/science/article/pii/S0022169420308593`, doi:`https://doi.org/10.1016/j.jhydrol.2020.125399`.

Trinchero, P., Puigdomenech, I., Molinero, J., Ebrahimi, H., Gylling, B., Svensson, U., Bosbach, D., Deissmann, G., 2017. Continuum-based DFN-consistent numerical framework for the simulation of oxygen infiltration into fractured crystalline rocks. Journal of Contaminant Hydrology 200, 60–69. doi:`10.1016/j.jconhyd.2017.04.001`.

Trinchero, P., Sidborn, M., Puigdomenech, I., Iraola, A., Bosbach, D., Deissmann, G., 2019a. Groundwater age dating in fractured rock using ^{4}He data. Journal of Hydrology X 4, 100036. URL: `http://www.sciencedirect.com/science/article/pii/S2589915519300203`, doi:`https://doi.org/10.1016/j.hydroa.2019.100036`.

Trinchero, P., Sidborn, M., Puigdomenech, I., Svensson, U., Ebrahimi, H., Molinero, J., Gylling, B., Bosbach, D., Deissmann, G., 2019b.

Transport of oxygen into granitic rocks: Role of physical and mineralogical heterogeneity. Journal of Contaminant Hydrology 220, 108–118. URL: https://www.sciencedirect.com/science/article/pii/S0169772218303838, doi:https://doi.org/10.1016/j.jconhyd.2018.12.001.

Vidstrand, P., Follin, S., Zugec, N., 2010. Groundwater flow modelling of periods with periglacial and glacial climate conditions–Forsmark. Technical Report R-09-21. Svensk KÃ¤rnbrÃ¤nslehantering AB (SKB), Stockholm, Sweden.

Wang, H., Xu, C., Dowd, P.A., Wang, Z., Faulkner, L., 2022a. Modelling in-situ recovery (ISR) of copper at the Kapunda mine, Australia. Minerals Engineering 186, 107752. URL: https://www.sciencedirect.com/science/article/pii/S0892687522003624, doi:https://doi.org/10.1016/j.mineng.2022.107752.

Wang, J., Carrera, J., Saaltink, M.W., Valhondo, C., 2022b. A general and efficient numerical solution of reactive transport with multirate mass transfer. Computers & Geosciences 158, 104953. URL: https://www.sciencedirect.com/science/article/pii/S0098300421002399, doi:https://doi.org/10.1016/j.cageo.2021.104953.

Wogelius, R.A., Milodowski, A.E., Field, L.P., Metcalfe, R., Lowe, T., van Veelen, A., Carpenter, G., Norris, S., Yardley, B., 2020. Mineral reaction kinetics constrain the length scale of rock matrix diffusion. Scientific Reports 10, 8142. URL: https://doi.org/10.1038/s41598-020-65113-x, doi:10.1038/s41598-020-65113-x.

Xu, T., Sonnenthal, E., Spycher, N., Pruess, K., 2006. TOUGHREACT - a simulation program for non-isothermal multiphase reactive geochemical transport in variably saturated geologic media: applications to geothermal injectivity and CO_2 geological sequestration. Computers & Geosciences 32, 145–165.

Symbol	Quantity	Value	Unit
b^{UF}	Half fracture aperture	$1.58 \cdot 10^{-3}$	m
b^{DF}		$3.16 \cdot 10^{-3}$	
Δ_m	Half fracture spacing	$9.80 \cdot 10^{-2}$	m
L	Length of each fracture	0.25	m
φ_m	Matrix porosity	$1.0 \cdot 10^{-2}$	-
D^f	Fracture diffusion coefficient	$1.0 \cdot 10^{-9}$	m^2/s
D^m	Matrix pore diffusion coefficient	$1.0 \cdot 10^{-10}$	m^2/s

Table 1: Parameters of the Verification Exercise. Super-scripts *UF* and *DF* indicate, respectively, the upstream and downstream fractures.

Symbol	Quantity	Value	Unit
ϵ^{UF}	Fracture volume fraction	$1.59 \cdot 10^{-2}$	-
ϵ^{DF}		$3.18 \cdot 10^{-2}$	
k_{eq}^{UF}	Permeability	$3.35 \cdot 10^{-9}$	m^2
k_{eq}^{DF}		$2.68 \cdot 10^{-8}$	
μ	Dynamic viscosity	$8.89 \cdot 10^{-4}$	Pa·s
$\frac{dp}{dx}$	Hydraulic gradient	$3.2 \cdot 10^{-3}$	Pa/m

Table 2: Verification exercise. Parameters of the ECPM dual-continuum model used for the TC. Super-scripts *UF* and *DF* indicate, respectively, the upstream and downstream fractures. The hydraulic gradient is from inlet to outlet fracture boundary.

Symbol	Quantity	Value	Unit
τ^{UF} τ^{DF}	Groundwater travel time	$5.9 \cdot 10^{-3}$ $1.2 \cdot 10^{-2}$	y
v^{UF} v^{DF}	Groundwater velocity	42.4 20.8	m/y
α	Longitudinal dispersivity	$2.5 \cdot 10^{-3}$	m

Table 3: Verification Exercise. Parameters used for the Sudicky's solution.

Parameter	Set 1	Set 2	Set 3	Set 4
Length interval [m]	15-1000			
Intensity I [m^{-3}]	$5.0 \cdot 10^{-2}$	$8.0 \cdot 10^{-2}$	$6.1 \cdot 10^{-2}$	$1.3 \cdot 10^{-1}$
Aperture [m]	$1.0 \cdot 10^{-4}$			
Power law exponent a [-]	-2.6	-2.5	-2.7	-2.7
λ_1 [-]	4.0	-4.9	-7.7	0.8
λ_2 [-]	-8.7	-11.0	0.02	0.8
λ_3 [-]	-0.6	-0.3	-1.1	-12.0

Table 4: Parameters of the DFN used in the large-scale applications (adapted from Vidstrand et al. (2010)).

Parameter	Set 1	Set 2	Set 3	Set 4
a_T [m^2/s]	$4.5 \cdot 10^{-7}$	$2.2 \cdot 10^{-6}$	$2.2 \cdot 10^{-6}$	$2.5 \cdot 10^{-6}$
b_T [-]	0.5	0.6	0.6	0.7
d_T [-]	0.8	1.4	1.0	1.4

Table 5: Coefficients of the power-law function used to generate fracture transmissivity in the large-scale applications (Eq. (21)) (adapted from Vidstrand et al. (2010)).

Symbol	Quantity	Value	Unit
ϕ^m	Matrix porosity	$1.0 \cdot 10^{-2}$	-
D^m	Matrix pore diffusion coefficient	$1.0 \cdot 10^{-10}$	m^2/s
S^m	Helium-4 bulk production rate*	$1.6 \cdot 10^{-15}$	mol / m^3 s

Table 6: Parameters of the secondary continuum (rock matrix) used in the synthetic large-scale applications. The asterisk identifies the parameter that is used only in application#1.

Species	Boundary water [mol/L]	Resident water [mol/L]
H^+	$1.0 \cdot 10^{-5}$	$1.0 \cdot 10^{-8}$
HCO_3^-	$1.0 \cdot 10^{-3}$	$1.7 \cdot 10^{-3}$
Ca^{2+}	$1.0 \cdot 10^{-6}$	$5.2 \cdot 10^{-4}$

Table 7: Composition of the resident and boundary water used in application#2. The initial concentration of calcium of the resident water has been obtained by equilibrating with calcite while the initial concentration of bicarbonate has been obtained by equilibrating with CO_2 with a partial pressure of $1.0 \cdot 10^{-3}$ bar.

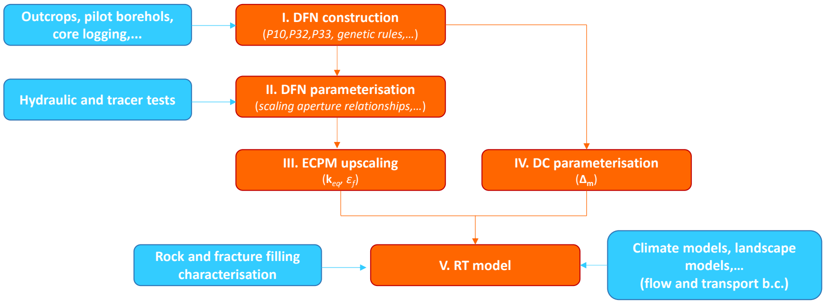

Figure 1: Flowchart showing the different steps required for the implementation and deployment of reactive transport models in the framework of long term safety assessment studies for nuclear waste disposal in fractured crystalline rock. Blue boxes refer to supporting studies or models from companion disciplines. These different acronyms are used: DFN (Discrete Fracture Network), ECPM (Equivalent Continuos Porous Media), DC (Dual-Continuum), RT (Reactive Transport).

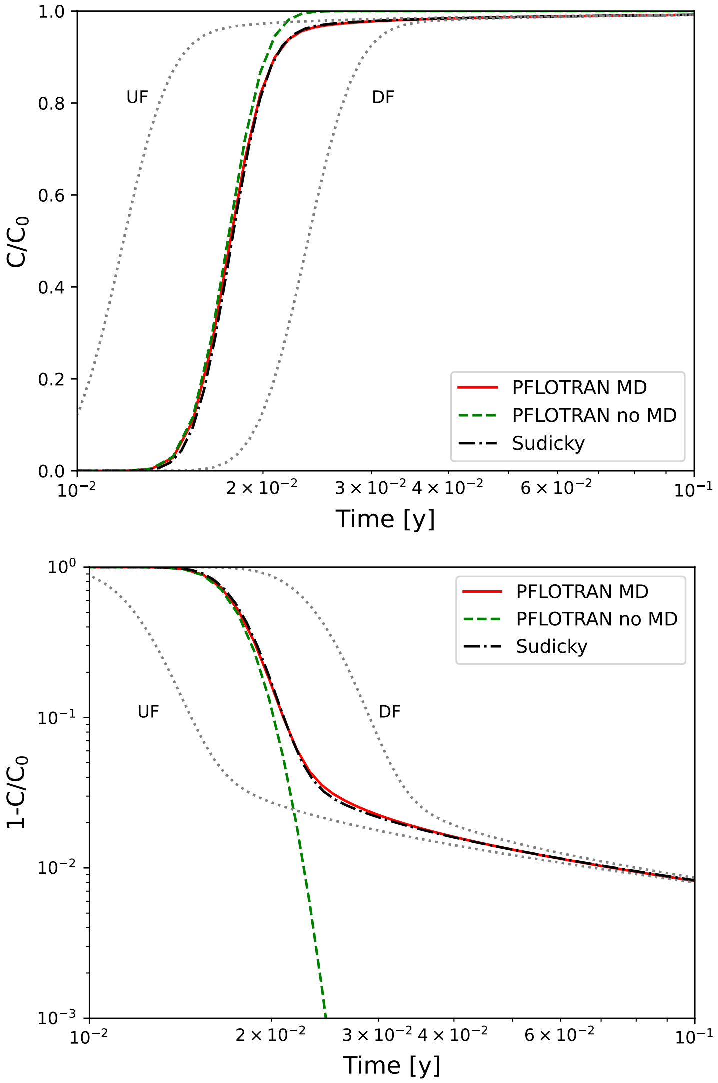

Figure 2: Verification Exercise. Breakthrough curves computed at the outlet boundary of the downstream fracture and shown on a (top) semi-log plot of normalised concentration (C/C_0) and (bottom) logaritmic plot of $1 - C/C_0$ to emphasise the long tail. The results of the two PFLOTRAN models (with matrix diffusion, "PFLOTRAN MD", and without matrix diffusion, "PFLOTRAN no MD") and the Sudicky's solution are shown with, respectively, continuous, dashed and dash-dotted lines. Two bounding solutions, which are plotted with dotted lines, show the breakthrough curves at the outlet of a homogeneous fracture-segment of length 0.5 m and with flow parameters (travel time and groundwater velocity) equal to either the upstream or the downstream fracture (see Table 3)).

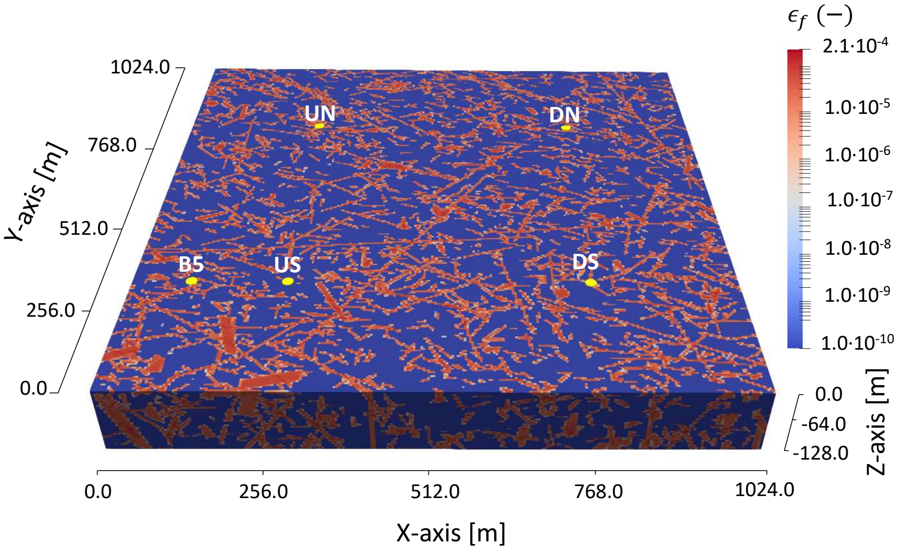

Figure 3: Distribution of fracture volume fraction (ϵ_f) for the large-scale model. The four boreholes used in aplication#1 (UN, US, DN and DS) and the borehole used in application#2 are also shown.

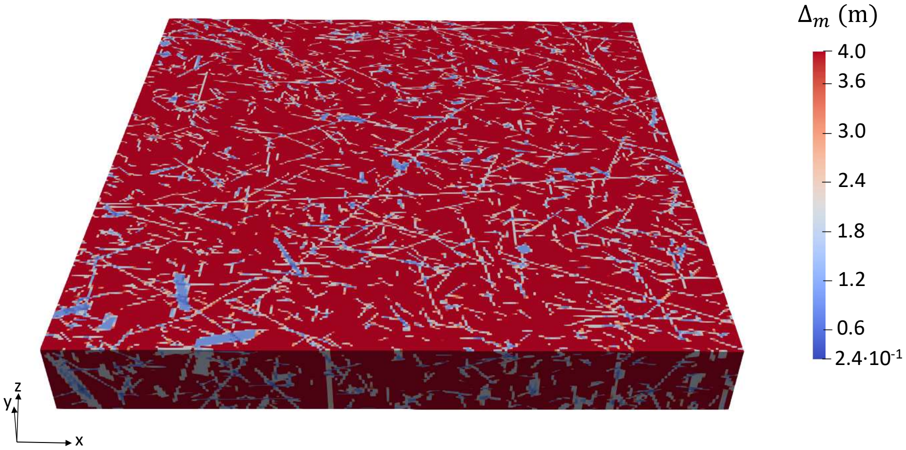

Figure 4: Distribution of matrix length for the large-scale model.

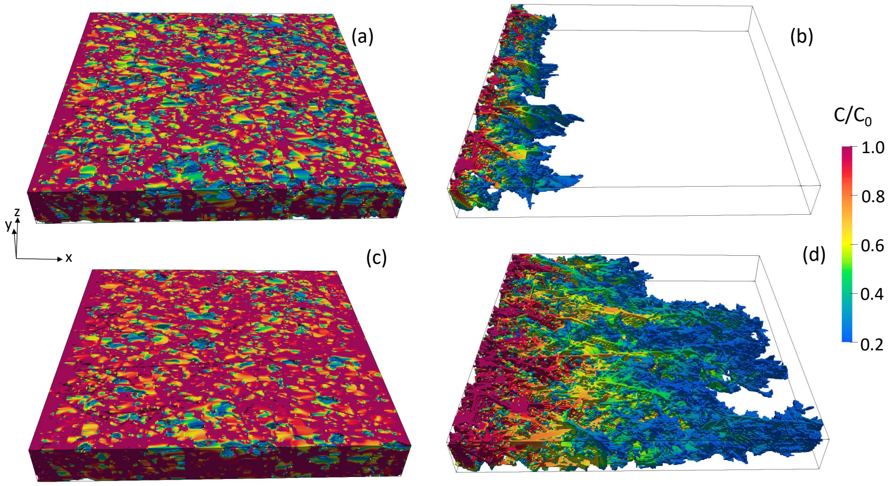

Figure 5: Concentration of a conservative tracer at time 1,000 y (top row) and 10,000 y (bottom row) for the model without ((a) and (c)) and with ((b) and (d)) matrix diffusion. Only cells with $c/c_0 > 0.2$ are shown.

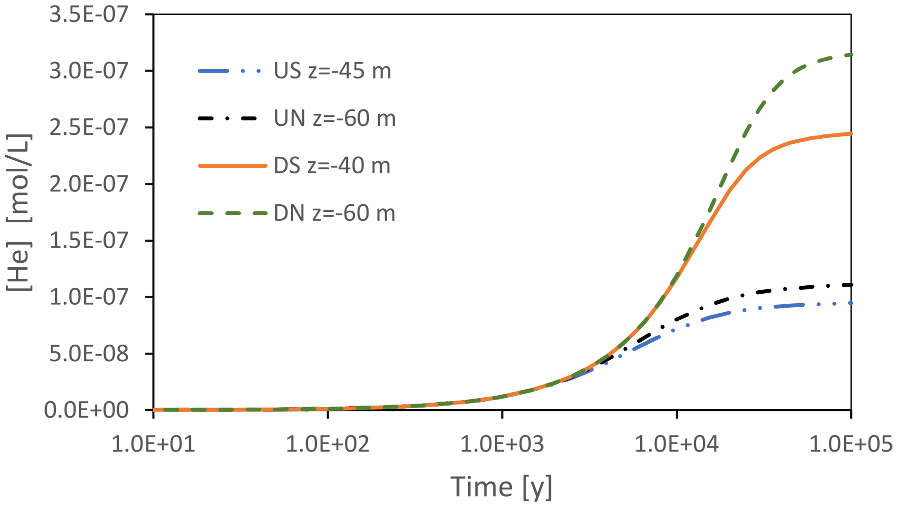

Figure 6: Helium brekthrough curves in four randomly selected packed-off sections. The acronyms of the four boreholes are according to the notation in Figure 3. The depth of each section is specified in the legend, with z=0 m being the location of the plane coinciding with the upper boundary of the modelled domain.

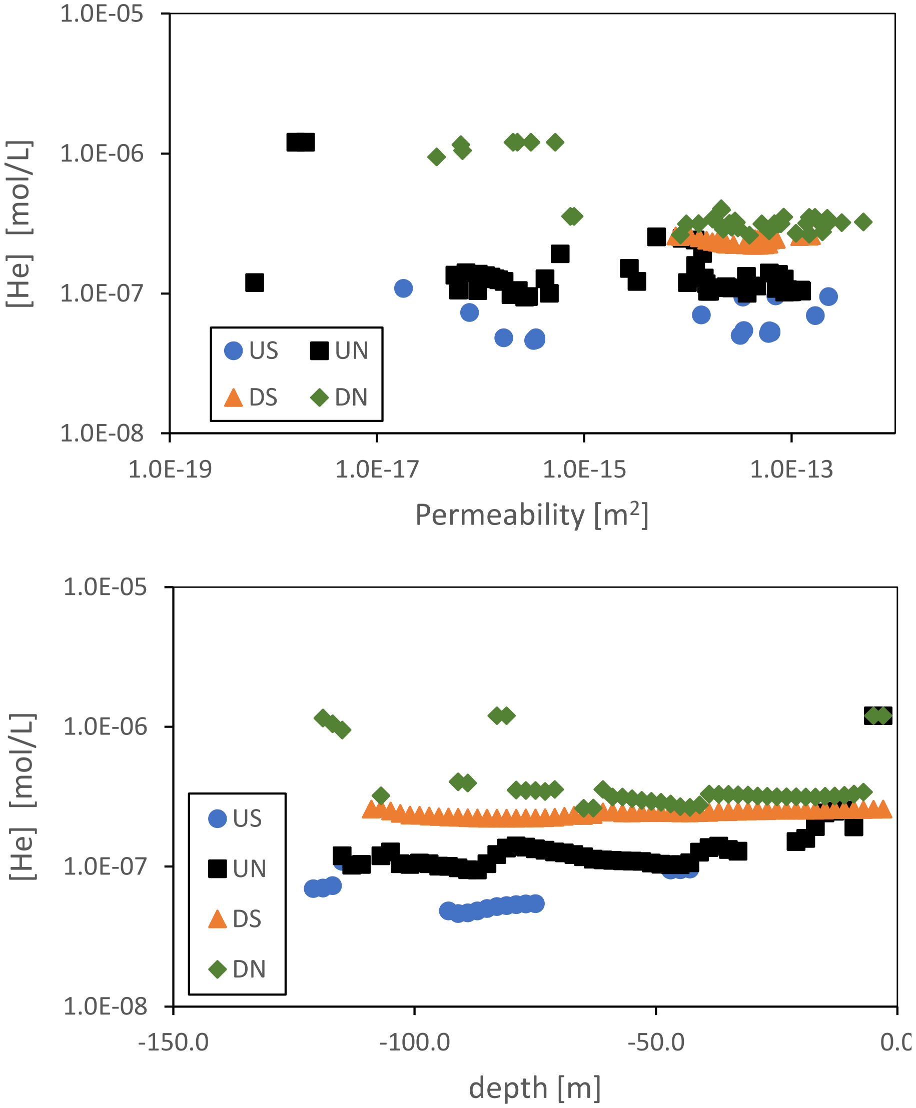

Figure 7: Helium concentration at the final simulation time (t=10^5 y) versus (a) local permeability and (b) depth. Each dot represents a packed-off section of 2 m length. Only the transmissive sections are represented ($\kappa > 1 \cdot 10^{-15}$ m^2). The acronyms of the four boreholes are according to the notation in Figure 3.

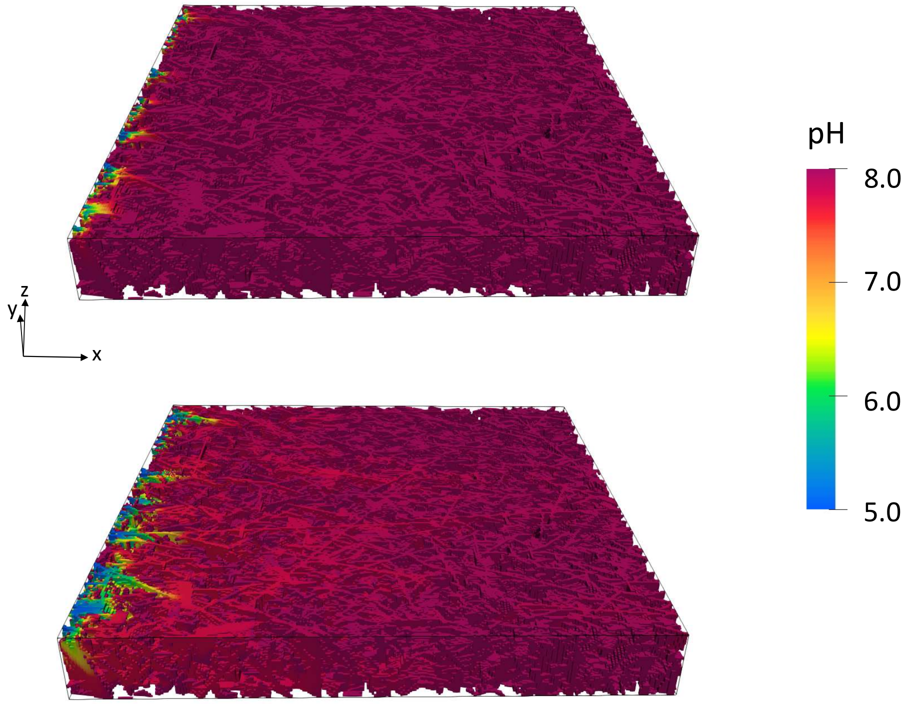

Figure 8: Application #2: pH at (top) 100 y and (bottom) 10,000 y.

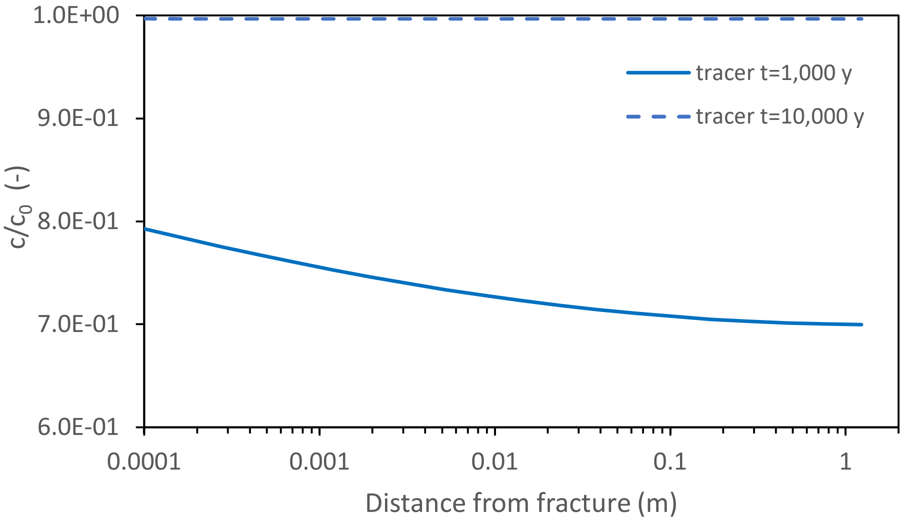

Figure 9: Application #2: profiles of tracer concentration in the rock matrix computed at 1,000 y (continuos line) and 10,000 y (dashed line) in borehole B5 (Figure 3) at depth -45 meters. The concentration is normalised by the concentration in the inlet.

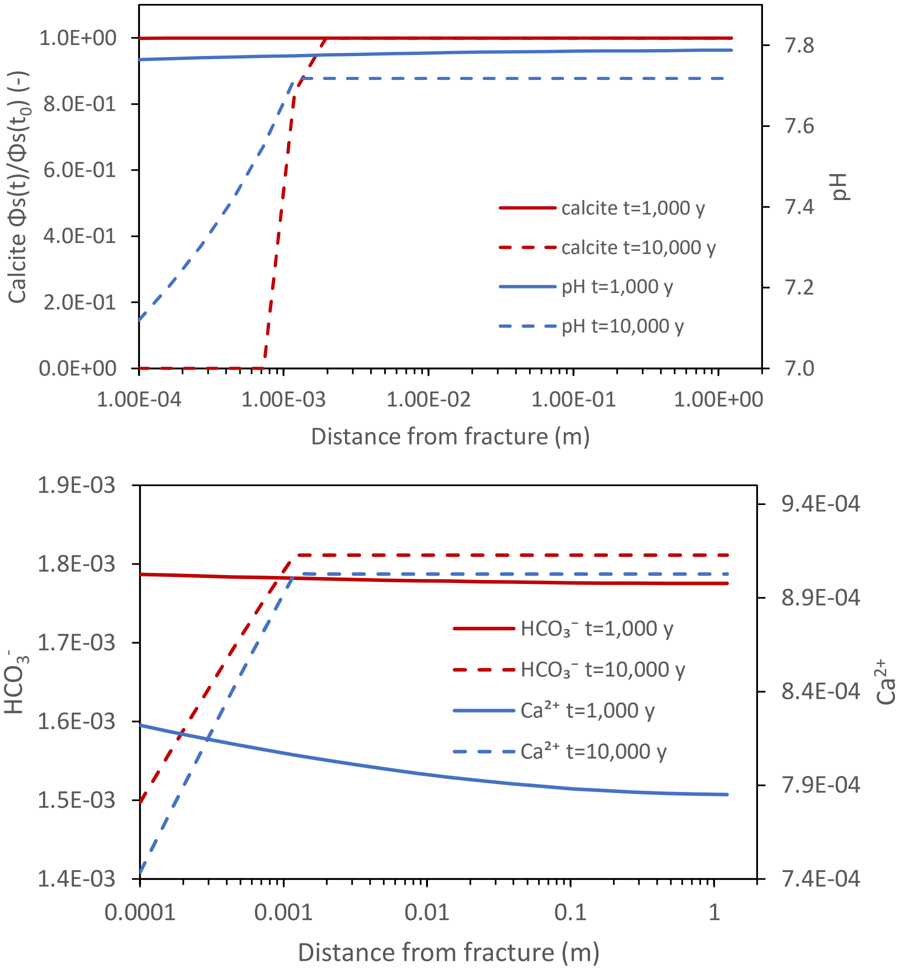

Figure 10: Application #2: profiles of (top) pH (blue lines) and relative variation of calcite volume fraction (red lines) and (bottom) bicarbonate (blue line) and calcium (red line) concentration in the rock matrix computed at 1,000 y (continuous lines) and 10,000 y (dashed lines) in borehole B5 (Figure 3) at depth -45 meters.

Appendix A. Semi-analytical solution for n consecutive fractures

Sudicky and Frind (1982) developed an analytical solution for the problem of transient contaminant transport in a system of perfectly parallel fractures. The solution assumes that a constant concentration (c_0) is prescribed at the inlet of the flowing fracture (Dirichlet boundary condition) and describes the evolution of resident concentration at any monitoring point of the fracture. Although the solution is provided in geometric ordinary space, it is much more convenient to use here the solution as derived in Laplace space. Thus, considering a non-decaying non-sorbing solute, the solution reads:

$$\overline{c} = \frac{c_0}{s} \cdot \exp(\omega) \cdot \exp(\gamma) \tag{A.1}$$

where $\overline{c}$ is the Laplace transform of the resident concentration at the monitoring point.

The first term on the right-hand side of Eq. A.5 represents the Laplace transform of the Dirichlet boundary condition and s is the Laplace variable. The arguments of the two exponential functions are:

$$\omega = \frac{\tau}{2\left(\alpha + D_m/v\right)} \tag{A.2}$$

and

$$\gamma = -\omega \left\{ 1 + \frac{4\left(D_m + \alpha v\right)}{v^2} \left[\frac{\sqrt{s}\kappa}{b} \tanh\left(\sqrt{\frac{s}{D_p}} \Delta + s \right) \right] \right\}^{1/2} \tag{A.3}$$

where τ [y] is the groundwater travel time from the inlet to the monitoring point in the fracture, v [m/y] is the groundwater velocity, α [m] is the longitudinal dispersivity, D_m [m^2/y] is the molecular diffusion coefficient in pure water, Δ [m] is the matrix length and κ is a material parameter group defined as:

$$\kappa = \varphi \sqrt{D_p} \tag{A.4}$$

where φ [-] is the matrix porosity and D_p [m^2/y] is the pore diffusion coefficient in matrix.

For n consecutive fractures, the breakthrough curve at the end of the n-th fracture can be computed as:

$$\bar{c} = \frac{c_0}{s} \cdot \exp(\omega_1) \cdot \exp(\gamma_1) \cdot \ldots \cdot \exp(\omega_n) \cdot \exp(\gamma_n) \tag{A.5}$$

The numerical inversion of the Laplace solution is here carried out using the De Hoog algorithm (De Hoog et al., 1982; Hollenbeck, 1998).

Appendix B. Verification of the two-fractures model against MARFA

The results of the PFLOTRAN calculation for the two fractures model (section 4) are here compared to a simulation carried out using the time-domain random walk computer code MARFA. The comparison was made in terms of mass flux (Ω [mol/y]) through the DF outlet normalised by mass flux at late times ($\Omega_\infty = \lim_{t\to\infty} \Omega(t)$). For the PFLOTRAN model, mass fluxes where computed using Eq.9a.

In MARFA, transport along a fracture is described by two hydrodynamic parameters: the groundwater travel time and the transport resistance; the latter is defined as (Cvetkovic et al., 1999):

$$\beta(\tau) = \int_0^\tau \frac{d\theta}{b\left(\theta\right)}, \tag{B.1}$$

where b is the fracture half-aperture and θ is a dummy integration variable. Neglecting fracture internal variability in openings, the transport resistance reduces to $\beta = \tau / b$.

The groundwater travel times of the two fracture segments as well as the longitudinal dispersivity used in the MARFA simulation are listed in Table 3, whereas the transport resistance was set equal to 3.72 y/m for both segments. Notice that $\beta^{UF} = \beta^{DF}$ since the wider aperture of the DF compensates its longer groundwater travel time.

The results of the comparison exercise are shown in Figure 3. The results of the dual-continuum ECPM model and the time-domain random walk simulation agree well. This provides a further verification of the DCDMM model.

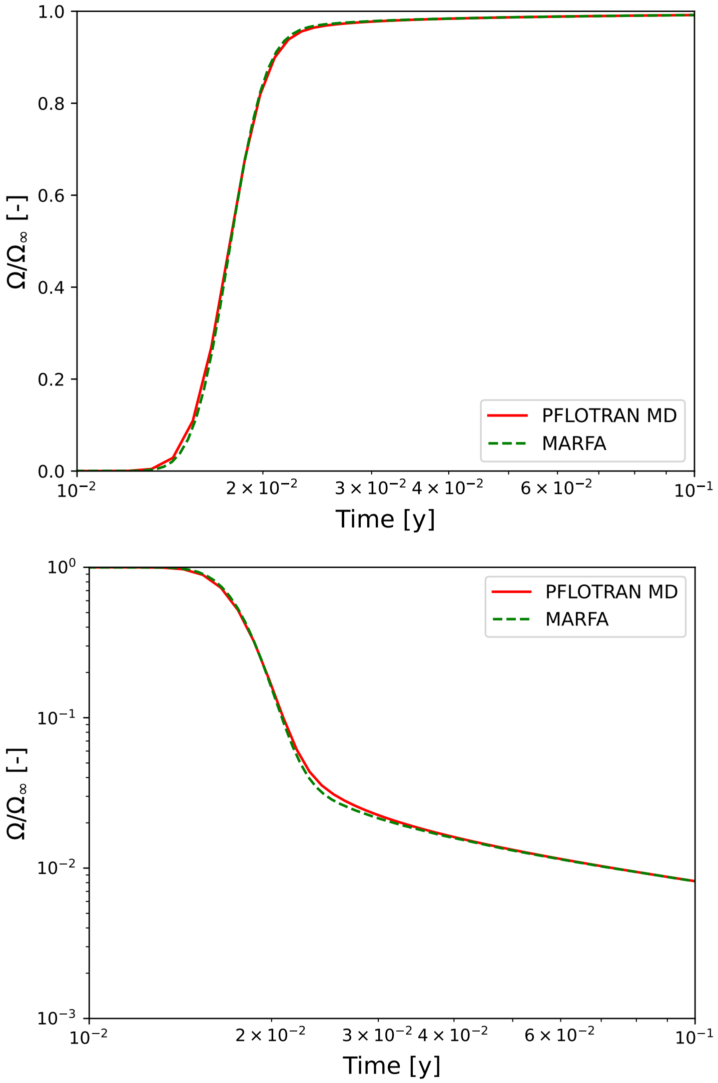

Figure B.11: Verification Exercise. Breakthrough curves computed at the outlet boundary of the downstream fracture and shown on a (top) semi-log plot of normalised mass flux (Ω/Ω_∞) and (bottom) logaritmic plot of $1 - \Omega/\Omega_\infty$ to emphasise the long tail. The results of the PFLOTRAN model ("PFLOTRAN MD" in the label) and the MARFA solution ("MARFA") are shown with, respectively, continuous and dashed lines.